# Facile Green Chemistry-Based Synthesis and Properties of Free-Standing Au− and Ag−PMMA Films

Muvva D. Prasad[†] and M. Ghanashyam Krishna*,[‡]

[†]UGC Networking Centre, School of Chemistry, and [‡]School of Physics, University of Hyderabad, Prof. C R Rao Road, Gachibowli, Hyderabad 500046, Andhra Pradesh, India

**ABSTRACT:** The synthesis of free-standing PMMA thin films by a green chemistry route and embedding them with Au and Ag nanoparticles is demonstrated. The fabrication involves the use of leaves of three different plants (*Syzygium cumini*, *Bauhinia purpurea*, and *Cymbopogon* (lemon grass)) on which the Ag- and Au-based precursors are deposited to realize the corresponding noble metal nanoparticles (NPs). The nanoparticle sizes are on the order of 10−20 nm. To achieve the free-standing films, the metal precursor is coated on leaf substrate followed by spin coating of a solution of PMMA polymer. After a short period of drying at room temperature, the polymer is peeled off from the leaf surface to get the free-standing thin film of noble metal−PMMA. Free-standing films of dimensions of 1.5 cm × 2.5 cm and thicknesses of several micrometers have been fabricated. The resultant films are shown to exhibit interesting plasmonic and catalytic properties.

**KEYWORDS:** *Free-standing films, PMMA, Au, Ag, Surface plasmons, Catalysis*
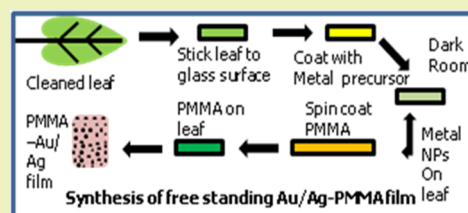
## ■ INTRODUCTION

Self-supported and free-standing thin films are extremely important for extending the applications of nanostructured materials. It has been shown that free-standing films can be used in a variety of technologies such as nanomembranes, supercapacitors, solar cells, energy storage, and photonics.[1−5] Apart from these, flexible electronics is another area where free-standing films will have a great impact.[6−10] Many of the reports involve very elaborate processes to realize the free-standing films. There is, thus, a need to develop facile synthesis routes to fabricate free-standing thin films for a variety of applications.

A number of techniques for the formation of noble metal−PMMA nanocomposites have been reported recently.[11−20] However, green chemistry routes for the synthesis of nanoparticles of noble metals (Au or Ag) and their nanocomposites with PMMA have also been the focus of intense research interest over the past few years because they afford the possibility of tuning plasmon resonances of the noble metals surface enhanced Raman spectra and also provide a platform for catalysis.[21−32] In fact, poly(methyl methacrylate) (PMMA) is a very popular material because it is both a thermoplastic and transparent plastic. It is frequently used as a low cost replacement for glass and is also preferred because of its moderate properties, ease of handling and processing. PMMA has therefore found application in medicine as lens implants, hard contact lenses, dentures, and electronics as an electron beam resist.[33−37] Hence, the motivation of the current work was fabrication of free-standing films of Au− and Ag−PMMA.

The objectives are to (1) synthesize free-standing PMMA thin films by a green chemistry route, without harsh processing conditions, and (2) embed Au and Ag nanoparticles on the PMMA surface. The fabrication involves leaves of three different plants (*Syzygium cumini*, *Bauhinia purpurea*, and
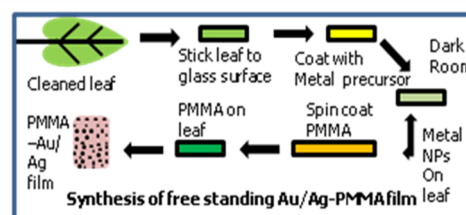


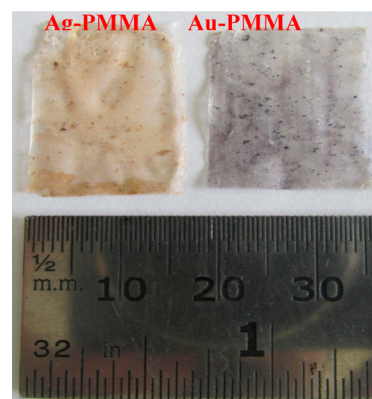**Figure 1.** Flowchart of the process used to obtain the free-standing films.



**Figure 2.** Photographs of the Au− and Ag−PMMA free-standing films.

*Cymbopogon* (lemon grass)) to synthesize the metal (Au and Ag) NPs. The metal precursor is coated on leaf substrate followed by spin coating of the PMMA polymer on the leaf surface. The polymer becomes dry after a short period of drying
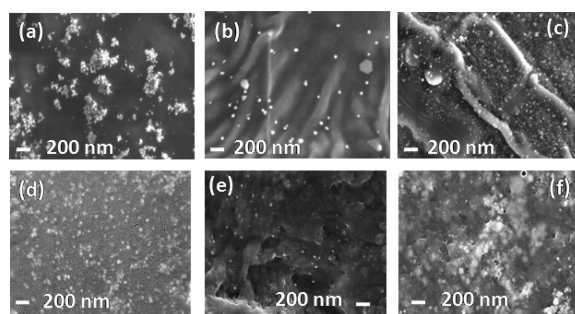
**Figure 3.** FE-SEM images of Au and Ag nanoparticles synthesized on the surface of (a,d) *S. cumini*, (b,e) *B. purpurea*, and (c,f) *Cymbopogon* leaf surfaces.
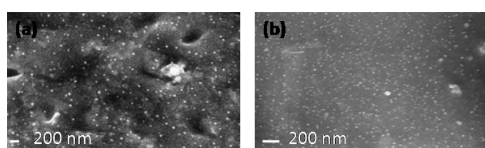


**Figure 4.** SEM images of the (a) Au−PMMA and (b) Ag−PMMA free-standing films.

at room temperature at which point it is peeled off from the leaf surface to get the free-standing thin film. The resultant films are then characterized for microstructure, structure, and optical properties.

## ■ MATERIALS AND METHODS

Three different plants (*Syzygium cumini*, *Bauhinia purpurea*, and *Cymbopogon* (lemon grass))) are used to synthesis the metal (Au and Ag) NPs. Leaves are plucked from these plants and cleaned thoroughly to removing the wax from the surface. To synthesize the Au nano-particles, 200 $\mu$L of 0.5, 1, and 2 mM HAuCl$_4$ and 200 $\mu$L of 2, 4, and 8 mM of AgNO$_3$ solutions are taken for Ag nanoparticles. The metal precursor (HAuCl$_4$ for Au and AgNO$_3$ for Ag) is then coated on leaf

substrate, which is stuck to a glass substrate to aid the coating process. The coated surfaces are then covered with a black cloth and stored in a dark room to avoid exposure to light. Upon drying, the leaf surface changes from green to brown color, indicating the formation of metal nanoparticles. This step is followed by spin coating of the PMMA polymer layer on the leaf surface. Polymethyl-methacrylate (PMMA: M.W.1, 20,000) solution was used for making a free-standing film with 1 g in 3 mL of chloroform (3.33 M). PMMA forms uniform film by spin coating on a leaf (at 500 rpm for 10 s followed by 2000 rpm for 10 s, using a Laurell Technologies Corporation Model WS-400B-6BOO/LITE/13K photoresist spinner). After drying for 5−10 min at room temperature, the polymer layer is peeled off along with the metal nanoparticles to obtain the free-standing thin film. The flowchart of the process to realize the free-standing film is shown in Figure 1. The photographs of the Au− and Ag−PMMA free-standing films are shown in Figure 2.

The films were then characterized for microstructure, structure, optical, and catalyst behavior. Scanning electron micrograph imaging was carried out with a field emission scanning electron microscope (FE-SEM, Model Ultra55, Carl Zeiss, Germany) using a 30 keV elec-tron beam. Transmission electron micrographs were obtained in a Tecnai 20 G2 STwin, FEI electron microscope, operated at 200 kV. Electron diffraction patterns (EDPs) were recorded with a Gatan CCD camera. A 10 nm gold film deposited on the grid was used for purpose of camera length calibration. The samples for TEM measurement were prepared by scratching the film and transferring it onto the grid. The optical absorption spectra were recorded in a UV−vis−NIR spectrophotmeter (JASCO Model V570) in the wavelength range between 190 and 2500 nm (only the relevant portions of the spectra are, however, presented). The free-standing film of Au and Ag films were stuck to a glass surface of 1.5 cm × 2.5 cm dimensions. The atomic force microscopy (AFM) images were then obtained on these surfaces in a NT-MDT Solver Pro M AFM in sem-contact mode using a cantilever with a force constant of 5.5−22.5 N/m. The gold-coated silicon probes had the following dimensions: chip size, 3.6 × 1.6 × 0.4 mm; radius of curvature, 10 nm; tip height, 10−15 $\mu$m. The images were analyzed by using Nova software. Metal-coated PMMA films were stuck to the glass surface and fixed to a sample stub. X-ray diffraction data was collected in a diffractometer (Bruker D8 advance X-ray diffractometer) using Cu K$\alpha$ radiation ($\lambda$ = 1.5406 Å) at 40 kV
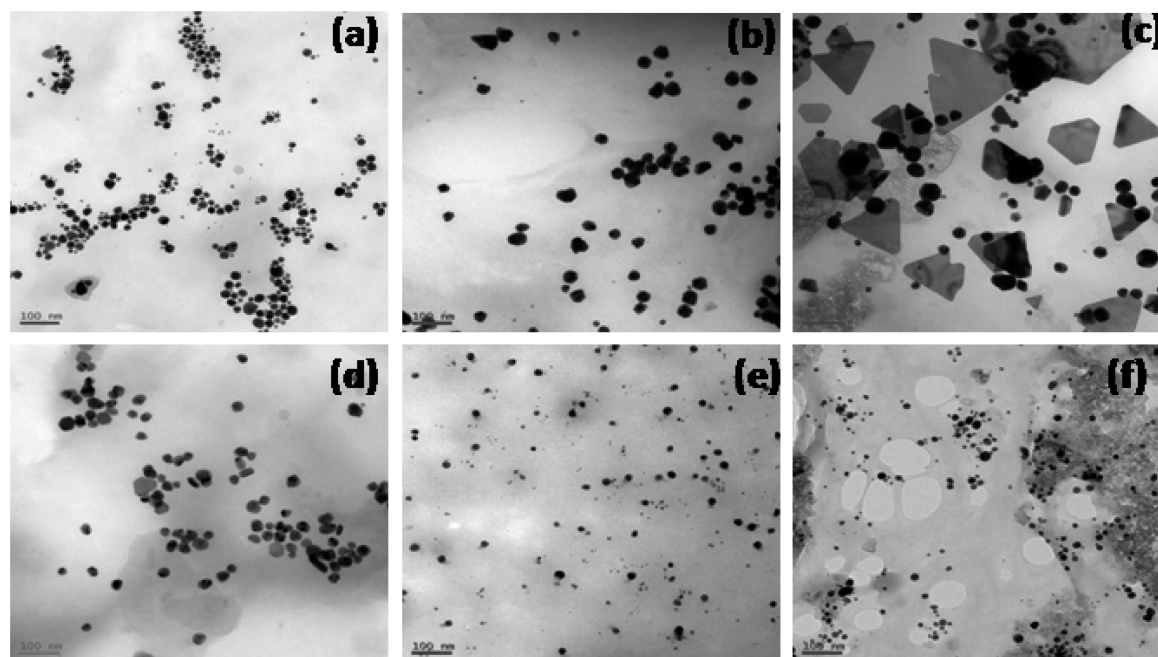


**Figure 5.** TEM images of Au and Ag nanoparticles transferred to the PMMA from the surface of (a,d) *S. cumini*, (b,e) *B. purpurea*, and (c,f) *Cymbopogon* leaf surfaces.
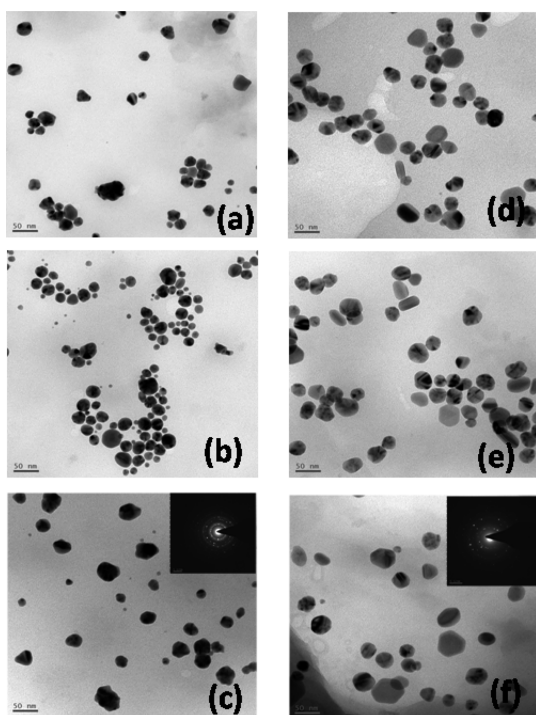
**Figure 6.** TEM images of (a) 0.5, (b) 1, and (c) 2 mM concentration of Au and (d) 2, (e) 4, and (f) 8 mM concentration of Ag nanoparticles on PMMA surfaces.



**Figure 8.** HRTEM images of (a) 0.5, (b) 1, and (c) 2 mM concentration of Au and (d) 2, (e) 4, and (f) 8 mM concentration of Ag nanoparticles on PMMA surfaces.

and 30 mA over a $2\theta$ range from 5° to 100°. Fourier transform infrared (FTIR) spectra were recorded in the range 4000 to 400 cm$^{-1}$ in a Thermo Scientific Nicolet 380 spectrometer.

## ■ RESULTS AND DISCUSSION

**Microstructure and Structure.** The morphological evolution of the Au and Ag nanoparticles is critically dependent on the substrate surface. The FE-SEM images shown in Figure 3 clearly demonstrate that there is clustering of Au nanoparticles on the *Syzygium* surface, whereas on the *Bauhinia* surface the wetting is very poor leading the nanoparticles with very large interparticle distance and consequently low surface coverage. On the surface of the *Cymbopogon* leaf, in contrast, there is uniform coverage of the particles. The differences in particle size, shape, and density can be attributed to the differences in the contact angle for wetting between the
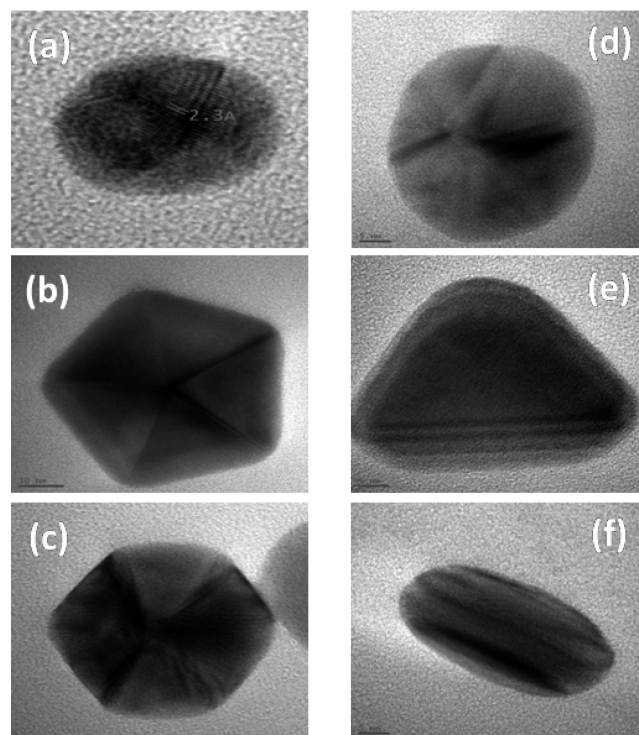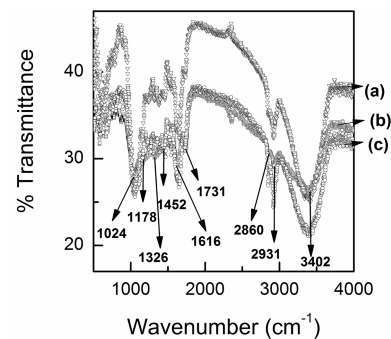


**Figure 9.** FTIR spectra of the three leaf surfaces (a) *Cymbopogon*, (b) *S. cumini*, and (c) *B. purpure*a.
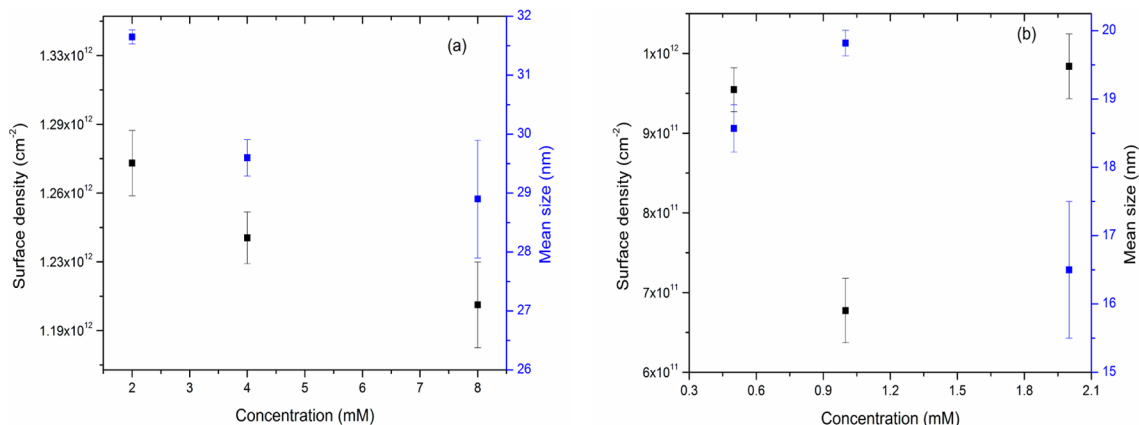


**Figure 7.** Variation of mean size and surface density of nanoparticles of (a) Ag and (b) Au with concentration.
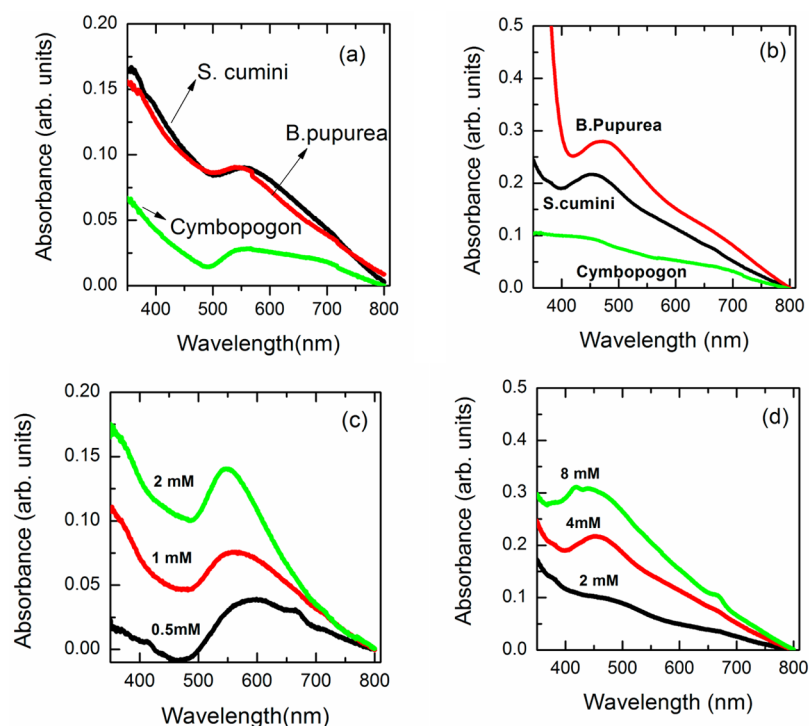
**Figure 10.** Optical absorption spectra of (a) Au nanoparticles on different leaves, (b) Ag nanoparticles on different leaves, (c) different concentrations of Au nanoparticles on *S. cumini*, and (d) different concentrations of Ag on *S. cumini*.

precursor solution and different leaf surfaces. Presumably, the contact angle is high in the case of the *Syzgium* surface and lowest in the case of the *Cymbopogon* leaf for the gold precursor. A similar situation applies for the Ag precursor as shown in Figure 3d−f. The SEM images of the Au and Ag PMMA surfaces are shown in Figure 4a and b, respectively.

The role of the leaf surface on Au and Ag nanoparticle size and shape is demonstrated in the TEM images displayed in Figure 5a−f. The Au particles transferred from the *Syzygium* surface continue to be spherical with sizes of the order of 10−20 nm. The particles transferred from the *Bauhinia* surface appear to agglomerate leading to an increase in their size to 30−40 nm. In the case of *Cymbopogon* leaf, the particle shape changes to large triangles, some of which are almost 100 nm on side. Evidently, there is a memory effect of the initial substrate surface on the Au particle shape and size when they are transferred onto the PMMA surface. In the case of Ag, however, as shown in Figure 5d−f, the particle shape is spherical, and the size is between 10 and 20 nm in all cases. The difference in behavior can be attributed to the differences between the Ag−leaf and Au−leaf interface.

The possibility of controlling size and shape of the particles by varying concentration is demonstrated in Figure 6a−c for Au and Figure 6d−f for Ag nanoparticles. In the case of Au, as shown in Figure 6a−c, with an increase in concentration from 0.5 to 2 mM, there is an increase in average size of nanoparticles from 2 to 35 nm. It is apparent that there is clustering of particles as a consequence of the increase in concentration. Another result of the clustering is also the crystallization of the nanoparticles as evidenced from the selected area electron diffraction (SAED) pattern displayed in the inset of Figure 6c. The average size of nanoparticles at 0.5, 1.0, and 2 mM concentration is 18.6 (±1.5), 19.8 (±1.5), and 16.5 (±3.5) nm, respectively.

Similar to Au, even in the case of Ag nanoparticles, there is an increase in size with an increase in concentration as observed from Figure 6d−f. However, there are some significant differences. First, the size of the Ag nanoparticles at 2 mM concentration is much larger (20−30 nm) in comparison to the Au nanoparticles. The mean sizes of the nanoparticles are 31.6 (±0.5), 29.6 (±0.6), and 28.9 (±0.9) nm at 2, 4, and 8 mM concentrations, respectively.

Second, a further increase in concentration results not only in an increase in the number of larger-sized (to 50−60 nm) particles but also in a change in shape into nanorods. At 8 mM concentration, the particles increase in size to >100 nm, and the particles change shape into hexagons and large spheres. This is accompanied by a decrease particle density leading to the inference that changes in shape can be attributed to clustering as a result of an increase in concentration. The crystallinity of the Ag nanoparticles is evident from the SAED pattern displayed in the inset of Figure 6f. The variation in the mean particle size and surface density with concentration is made and shown in Figure 7a and b for Ag and Au, respectively. It is evident that there is a strong correlation between the concentration and size as well as surface density in both cases. Closer examination of the particles by high resolution TEM in Figure 8a−c for Au and Figure 8d−f for Ag, show that there is faceting of the particles with an increase in concentration. In the case of Au, the particles are conical at 0.5 mM with a large ellipsoidal base and short apex. With a further increase in concentration, the shapes change to pentagonal and hexagonal pyramids at 1 and 2 mM, respectively. In the case of Ag particles, again the conical particles initially transform into layered triangles at 4 mM and finally into nanorods at 8 mM.

To identify the possible functional groups involved in the bioreduction, FT-IR spectra of the leaf surfaces used as substrates were recorded, and these are displayed in Figure 9(a−c)
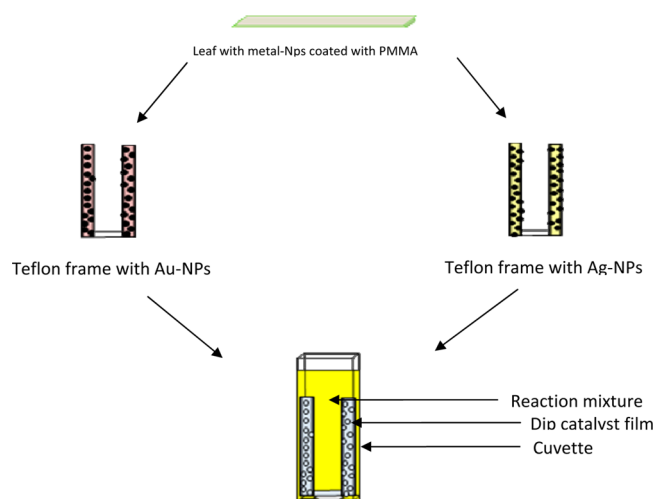
**Figure 11.** Schematic of the process to form a "dip catalyst".

for *Cymbopogon*, *S.cumini*, and *B. purpurea*, respectively. However, only the peak positions for *S. cumini* are indicated in the figure. The FT-IR spectra show the presence of absorption bands around 3402 cm$^{-1}$ due to the stretching of the N−H group of amino and hydroxyl(−OH) group. Strong absorption peaks at wavenumbers around 2860 and 2931 cm$^{-1}$ represent the C−H bonded stretching of alkanes. The shoulder at 1731 cm$^{-1}$ is characteristic of carbonyl stretching in ketones, aldehydes, and carboxylic acids. The absorption peaks at 1616 and 1452 cm$^{-1}$ represent the aromatic C=C stretching in carboxyl coupled to the amide linkage of amide I. The shoulder around 1326 cm$^{-1}$ represents the asymmetrical stretching of nitro compounds. The peaks at 1024 and 1178 cm$^{-1}$ are due to the stretching of C−O for the secondary alcohols, ethers, carboxylic acid, and ester groups present. The above-mentioned wavenumbers correspond to *S. cumini* only, and it is pertinent to note that there is a slight shift in the wavenumbers on the other leaf surfaces.

It is evident from the results presented that the synthesis process allows tunability of shape and size of particles over a large range. Two applications of the free-standing films (1) for surface plasmon resonance-based devices and (2) catalysis are demonstrated in the next two sections

## SURFACE PLASMON RESONANCE

Surface plasmon resonances (SPR) of noble metal particles are known to be extremely sensitive to both shape and size of
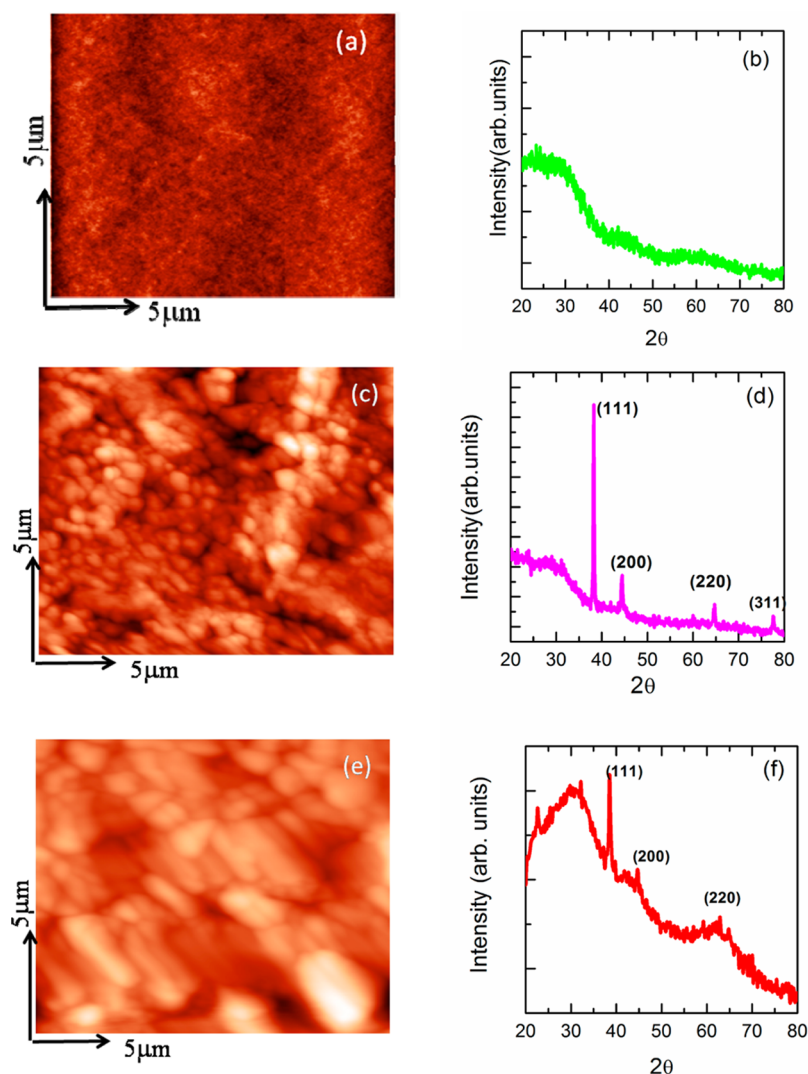


**Figure 12.** AFM images and X-ray diffraction patterns, respectively, of (a),(b) PMMA surface, (c),(d) Au−PMMA, and (e),(f) Ag−PMMA free-standing films.
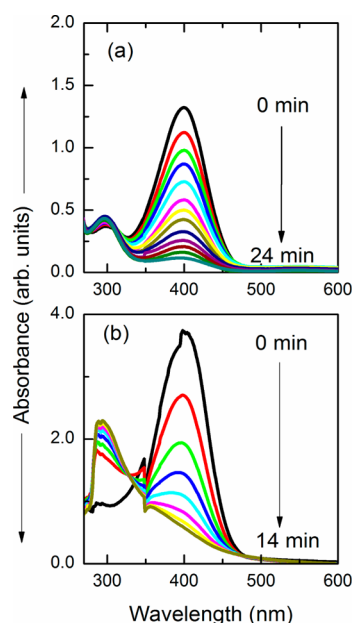
**Figure 13.** Variation in intensity of the 380 nm peak as a function of time for (a) Au and (b) Ag.
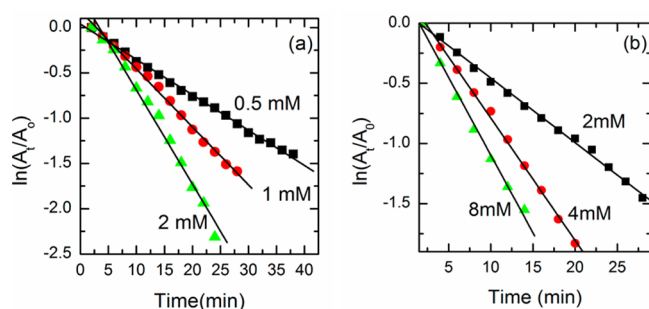


**Figure 14.** Variation of $\ln(A_t/A_0)$ (as defined in the text) as a function of time for (a) Au and (b) Ag at different concentrations.

particles. The SPR spectra of the Au particles deposited on the three different leaf surfaces is shown in Figure 10a. The resonance peak occurs at 545 nm for Au nanoparticles on all the three leaves. The SPR peak is broad and weak. In the case of Ag on the different leaves (Figure 10b) on *S.cumini* and *B. purpurea*, it occurs around 480 nm, whereas on *Cymbopogon* (lemon grass) the peak is very weak. After formation of the Au−PMMA free-standing film, the SPR peak shows a strong dependence on concentration with a broad peak centered around 570 nm at a concentration of 0.5 mM (Figure 10c). This peak blue shifts to 550 nm with an increase in concentration to 2 mM. Thus, with an increase in concentration, there is a narrowing of peak width that is accompanied by a blue shift in the peak position. In the case of Ag, as observed in

Figure 10c, the 2 mM concentration films displays a very weak resonance that with an increase in concentration to 8 mM shows a blue shift and well-defined resonance at 450 nm. At 8 mM concentration, there is a further blue shift and narrowing of the peak that is now centered around 430 nm.

Clearly, the SPR can be tuned and the variations can be correlated with changes in shape and size of particles. The large width of the peak and blue shift, although there is increase in size, indicates that the variations are shape related. The effect of different dielectric environments around the nanoparticles can also be responsible for the observed changes. It has been reported by other workers that localized SPR peak positions are more sensitive to changes in shape than differences in size.[37]

## CATALYTIC PROPERTIES

The catalytic behavior of the Au− and Ag−PMMA free-standing films is demonstrated by studying the reduction of 4-nitrophenol to 4-aminophenol. The schematic of the process to synthesize the free-standing films as "dip catalysts"[38,39] is shown in Figure 11.

The atomic force microscopy images of the PMMA surface and Au− and Ag−PMMA free-standing films along with the corresponding X-ray diffraction patterns are shown in Figure 12a−f. The bare PMMA surface is smooth and amorphous (Figure 12a).

Both the Au− and Ag−PMMA free-standing films show submicrometer-sized aggregates with porosity that could be useful for catalytic applications. The X-ray diffraction patterns indicate that Au and Ag crystallize even at room temperature, which is significant from the perspective of applications

The free-standing Au− and Ag−PMMA films are immersed in the reaction mixture, and the reaction rate is then monitored by successive UV−vis absorption measurements by recording the intensity of the peak at 380 nm. It is evident from Figure 13a that the reduction in the case of Au is completed within 24 min as evidenced by the disappearance of the 430 nm SPR peak and appearance of the 380 nm absorption peak. In contrast, in the case of the Ag−PMMA film, the conversion is completed within 14 min as observed from Figure 13b.

To determine the rate constant of the variation in absorbance of the 4-NP ion, $\ln(A_t/A_0)$ is plotted as a function of time for Au and Ag nanoparticles extracted from the *S. cumini* leaf (Figure 14a and b), and the calculated rate constants are tabulated in Table 1. A good linear correlation is obtained both in the case of Au and Ag nanoparticles for all the concentrations studied, indicating that the reaction can be considered as a pseudo-first-order reaction. The calculated values of the catalytic rate constant ($k$) for Au and Ag shown in Table 1 show that the time for reaction to complete decreases with an increase in metal concentration, while the rate constant values increase as expected. There are many reports in the literature that state that both 4-nitrophenol and the reducing agent BH4

**Table 1. Catalytic Reaction Parameters Extracted from Figures 13 and 14**

|          |        | particle core size (nm) | size of the film | time for completion of reaction (min) | first-order rate constant ($k$, min$^{-1}$) | *p*-nitroaniline conversion (%) |
|----------|--------|-------------------------|------------------|---------------------------------------|---------------------------------------------|---------------------------------|
| Au−PMMA  | 0.5 mM | 18.6                    | 1.5 × 2.5 cm     | 30                                    | $2.3 \times 10^{-2}$                        | 76                              |
|          | 1 mM   | 19.8                    |                  | 28                                    | $3.5 \times 10^{-2}$                        | 79.4                            |
|          | 2 mM   | 16.5                    |                  | 24                                    | $9.3 \times 10^{-2}$                        | 91                              |
| Ag−PMMA  | 2 mM   | 31.6                    | 1.5 × 2.5 cm     | 30                                    | $2.5 \times 10^{-2}$                        | 78.6                            |
|          | 4 mM   | 29.6                    |                  | 20                                    | $2.8 \times 10^{-2}$                        | 84.2                            |
|          | 8 mM   | 28.9                    |                  | 14                                    | $4.9 \times 10^{-2}$                        | 90                              |

are adsorbed on the surface of the metal nanoparticles. The surface hydride ions are then transferred to 4-nitrophenol thereby facilitating the reduction reaction. The rate constant values compare very favorably with those reported earlier in literature.[40]

## ■ SUMMARY

In summary, a facile synthesis method for the fabrication of large-area free-standing films of Au− and Ag−PMMA has been demonstrated. The process does not involve high temperatures or harsh environments. It consists of forming the noble metal nanoparticles on leaf surfaces followed by spin coating of the PMMA leading to free-standing films by peeling off the noble metal−PMMA surface. The free-standing films are shown to exhibit interesting plasmonic and catalytic properties.

## ■ AUTHOR INFORMATION

**Corresponding Author**
*E-mail: mgksp@uohyd.ernet.in.
**Notes**
The authors declare no competing financial interest.

## ■ ACKNOWLEDGMENTS

## ■ REFERENCES

(1) Roberts, M. M.; Klein, L. J.; Savage, D. E.; Slinker, K. A.; Friesen, M.; Celler, G.; Eriksson, M. A.; Lagally, M. G. Elastically relaxed free-standing strained-silicon nanomembranes. *Nat. Mater.* **2006**, *5*, 388−393.

(2) Xu, D.; Xu, Q.; Wang, K.; Chen; Chen, Z. Fabrication of free-standing hierarchical carbon nanofiber/graphene oxide/polyaniline films for supercapacitors. *ACS Appl. Mater. Interfaces* **2014**, *6*, 200−209.

(3) Wang, L.; Xue, Z.; Liu, X.; Liu, B. Transfer of asymmetric free-standing TiO_2 nanowire films for high efficiency flexible dye-sensitized solar cells. *RSC Adv.* **2012**, *2*, 7656−7659.

(4) Kok, S. L.; White, N. M.; Harris, N. R. Fabrication and characterization of free-standing thick-film piezoelectric cantilevers for energy harvesting. *Meas. Sci. Technol.* **2009**, *20*, 124010−124016.

(5) Böcking, T.; Kilian, K. A.; Reece, P. J.; Gaus, K.; Gal, M.; Gooding, J. J. Biofunctionalization of free-standing porous silicon films for self-assembly of photonic devices. *Soft Matter* **2012**, *8*, 360−366.

(6) Park, J.; Kim, J.; Lee, S.; Bang, J.; Kim, B. J.; Kim, Y. S.; Cho, J. Free-standing film electronics using photo-crosslinking layer-by-layer assembly. *J. Mater. Chem.* **2009**, *19*, 4488−4490.

(7) Wang, C.; Hwang, D.; Yu, Z.; Takei, K.; Park, J.; Chen, T.; Ma, B.; Javey, A. User-interactive electronic skin for instantaneous pressure visualization. *Nat. Mater.* **2013**, *12*, 899−904.

(8) Kaltenbrunner, M.; White, M. S.; Głowacki, E. D.; Sekitani, T.; Someya, T.; Sariciftci, N. S. Ultrathin and lightweight organic solar cells with high flexibility. *Nature commun.* **2012**, *3*, 770−773.

(9) Nomura, K.; Ohta, H.; Takagi, A.; Kamiya, T.; Hirano, M.; Hosono, H. Room-temperature fabrication of transparent flexible thin-film transistors using amorphous oxide semiconductors. *Nature* **2004**, *432*, 488−492.

(10) Chien, C.-W.; Wu, C.-H.; Tsai, Y.-T.; Kung, Y.-C.; Lin, C.-Y.; Hsu, P.-C.; Hsieh, H.-H.; Wu, C.-C.; Yeh, Y.-H.; Leu, C.-M.; Lee, T.-M. High-performance flexible a-IGZO TFTs adopting stacked electrodes and transparent polyimide-based nanocomposite substrates. *IEEE Trans. Electron Devices* **2011**, *58*, 1440−1447.

(11) Ruffino, F.; Torrisi, V.; Marletta, G.; Grimaldi, M. G. Patterning of templated-confined nanoscale Au films by thermal-induced dewetting process of a poly(methylmethacrylate) underlying layer. *J. Appl. Phys.* **2012**, *112*, 124316.

(12) Ruffino, F.; Torrisi, V.; Marletta, G.; Grimaldi, M. G. Growth morphology of nanoscale sputter-deposited Au films on amorphous soft polymeric substrates. *Appl. Phys. A: Mater. Sci. Process.* **2011**, *103*, 939−949.

(13) Ruffino, F.; Torrisi, V.; Marletta, G.; Grimaldi, M. G. Effects of the embedding kinetics on the surface nano-morphology of nano-grained Au and Ag films on PS and PMMA layers annealed above the glass transition temperature. *Appl. Phys. A: Mater. Sci. Process.* **2012**, *107*, 669−683.

(14) Kaune, G.; Ruderer, M. A.; Metwalli, E.; Wang, W.; Couet, S.; Schlage, K.; Rohlsberger, R.; Roth, S. V.; Muller-Buschbaum, P. In situ GISAXS study of gold film growth on conducting polymer films. *ACS Appl. Mater. Interfaces* **2009**, *1*, 353−360.

(15) Buffet, A.; Mottakin, M.; Kashem, A.; Schlage, K.; Couet, S.; Rohlsberger, R.; Rothkirch, A.; Herzog, G.; Metwalli, E.; Meier, R.; Kaune, G.; Rawolle, M.; Muller-Buschbaum, P.; Gehrke, R.; Roth, S. V. Time-resolved ultrathin cobalt film growth on a colloidal polymer template. *Langmuir* **2011**, *27*, 343−346.

(16) Ruderer, M. A.; Körstgens, V.; Metwalli, E.; Al-Hussein, M.; Vainio, U.; Roth, S. V.; Döhrmann, R.; Gehrke, R.; Gebhardt, R.; Burghammer, M.; Müller-Buschbaum, P. Determination of the local gold contact morphology on a photoactive polymer film using nanobeam GISAXS. *Nucl. Instrum. Methods Phys. Res., Sect. B* **2010**, *268*, 403−410.

(17) Beyene, H. T.; Chakravadhanula, V. S. K.; Hanisch, C.; Strunskus, T.; Zaporojtchenko, V.; Elbahri, M.; Faupel, F. Vapor phase deposition, structure, and plasmonic properties of polymer-based composites containing Ag−Cu bimetallic nanoparticles. *Plasmonics* **2012**, *7*, 107−114.

(18) Peter, T.; Wegner, M.; Zaporojtchenko, V.; Strunskus, T.; Bornholdt, S.; Kersten, H.; Faupel, F. Metal/polymer nanocomposite thin films prepared by plasma polymerization and high pressure magnetron sputtering. *Surf. Coat. Technol.* **2011**, *205*, S38−S41.

(19) Faupel, F.; Zaporojtchenko, V.; Strunskus, T.; Elbahri, M. Metal-polymer nanocomposites for functional applications. *Adv. Eng. Mater.* **2010**, *12*, 1177−1190.

(20) Mishra, Y. K.; Mohapatra, S.; Chakravadhanula, V. S. K.; Lalla, N. P.; Zaporojtchenko, V.; Avasthi, D. K.; Faupel, F. Synthesis and characterization of Ag-polymer nanocomposites. *J. Nanosci. Nano-technol.* **2010**, *10*, 2833−2837.

(21) Iravani, S. Green synthesis of metal nanoparticles using plants. *Green Chem.* **2011**, *13*, 2638−2650.

(22) Hebbalalu, D.; Lalley, J.; Nadagouda, M. N.; Varma, R. S. Greener techniques for the synthesis of silver nanoparticles using plant extracts, enzymes, bacteria, biodegradable polymers, and microwaves. *ACS Sustainable Chem. Eng.* **2013**, *1*, 703−712.

(23) Song, J. Y.; Jang, H.-K.; Kim, B. S. Biological synthesis of gold nanoparticles using *Magnolia kobus* and *Diopyros kaki* leaf extracts. *Proc. Biochem.* **2009**, *44*, 1133−1138.

(24) Shiv Shankar, S.; Rai, A.; Ahmad, A.; Sastry, M. Rapid synthesis of Au, Ag, and bimetallic Au core−Ag shell nanoparticles using Neem (*Azadirachta indica*) leaf broth. *J. Colloid Interface Sci.* **2004**, *275*, 496−502.

(25) Gaware, U.; Kamble, V.; Ankamwar, B. Ecofriendly synthesis of anisotropic gold nanoparticles: A potential candidate of SERS Studies. *Int. J. Electrochem.* **2012**, DOI: 10.1155/2012/276246.

(26) Chandran, S. P.; Chaudhary, M.; Pasricha, R.; Ahmad, A.; Sastry, M. Synthesis of gold nanotriangles and silver nanoparticles using *Aloe vera* plant extract. *Biotechnol. Prog.* **2006**, *22*, 577−583.

(27) Shiv Shankar, S.; Rai, A.; Ankamwar, B.; Singh, A.; Ahmad, A.; Sastry, M. Biological synthesis of triangular gold nanoprisms. *Nat. Mater.* **2004**, *3*, 482−487.

(28) Kinnan, M. K.; Kachan, S.; Simmons, C. K.; Chumanov, G. Plasmon coupling in two-dimensional arrays of silver nanoparticles: I. Effect of the dielectric medium. *J. Phys. Chem. C* **2009**, *113*, 7079−7084.

(29) Grzelczak, M.; Perez-Juste, J.; Mulvaney, P.; Liz-Marzan, L. M. Shape control in gold nanoparticle synthesis. *Chem. Soc. Rev.* **2008**, *37*, 1783−1791.

(30) Alexandrov, A.; Smirnova, L.; Yakimovich, N.; Sapogova, N.; Soustov, L.; Kirsanov, A.; Bityurin, N. UV-initiated growth of gold nanoparticles in PMMA matrix. *Appl. Surf. Sci.* **2005**, *248*, 181−184.

(31) Yilmaz, E.; Suzer, S. Au nanoparticles in PMMA matrix: In situ synthesis and the effect of Au nanoparticles on PMMA conductivity. *Appl. Surf. Sci.* **2010**, *256*, 6630−6633.

(32) Kong, H.; Jang, J. Antibacterial properties of novel poly(methyl methacrylate) nanofiber containing silver nanoparticles. *Langmuir* **2008**, *24*, 2051−2056.

(33) Ravarian, R.; Zhong, X.; Barbeck, M.; Ghanaati, S.; Kirkpatrick, C. J.; Murphy, C. M.; Schindeler, A.; Chrzanowski, W.; Dehghani, F. Nanoscale chemical interaction enhances the physical properties of bioglass composites. *ACS Nano* **2013**, *7*, 8469−8483.

(34) Abuzar, M. A.; Bellur, S.; Duong, N.; Kim, B. B.; Lu, P.; Palfreyman, N.; Surendran, D.; Tran, V. T. Evaluating surface roughness of a polyamide denture base material in comparison with poly (methyl methacrylate). *J. Oral Sci.* **2010**, *52*, 577−581.

(35) Yasin, S.; Khalid, M. N.; Hasko, D. G. Reduction in roughness of resist features in PMMA due to the absence of a rinse. *Jpn. J. Appl. Phys.* **2004**, *43*, 6984−6987.

(36) McMahon, T. T.; Polse, K. A. Effects of long term extended wear of PMMA lenses on corneal function: a case report. *J. Am. Optom Assoc.* **1994**, *65*, 788−90.

(37) Bainbridge, J. W. B.; Teimory, M.; Tabandeh, H.; Kirwan, J.F.; Dalton, R.; Reid, F.; Rostron, C. K. Intraocular lens implants and risk of endophthalmitis. *Br. J. Ophthalmol* **1998**, *82*, 1312−1315.

(38) Hariprasad, E.; Radhakrishnan, T. P. A highly efficient and extensively reusable "dip catalyst" based on a silver-nanoparticle-embedded polymer thin film. *Chem.—Eur. J.* **2010**, *16*, 14378−14384.

(39) Hariprasad, E.; Radhakrishnan, T. P. Palladium nanoparticle-embedded polymer thin film "dip catalyst" for Suzuki−Miyaura reaction. *ACS Catal.* **2012**, *2*, 1179−1186.

(40) Reddy, V.; Torati, S. R.; Oh, S.; Kim, C. G. Biosynthesis of gold nanoparticles assisted by *Sapindus mukorossi* Gaertn. fruit pericarp and their catalytic application for the reduction of *p*-nitroaniline. *Ind. Eng. Chem. Res.* **2013**, *52*, 556−564.